Draft version April 16, 2026
Typeset using LaTeX **twocolumn** style in AASTeX631

Linking System of Jets to the Non-Gravitational Acceleration of 3I/ATLAS

Toni Scarmato[1] and Abraham Loeb[2]

[1] *Toni Scarmato's Astronomical Observatory, San Costantino di Briatico, Calabria, 89817, Italy*
[2] *Astronomy Department, Harvard University, 60 Garden Street, Cambridge MA 02138, USA*

ABSTRACT

Building on the jet morphology and periodic wobble analysis of 3I/ATLAS in Scarmato & Loeb (2026), we link observed jet position angles (PAs) and the non-gravitational acceleration components (A_1, A_2, A_3) in the 3D RTN (radial, transverse, normal) frame relative to the Sun. We: (i) compute RTN directions from heliocentric state vectors and project them on the sky at the measured astrometric pointings; (ii) compare projected RTN PAs to three persistent jets (Jet1-Jet2-Jet3) and quantify angular offsets; and (iii) estimate order-of-magnitude thrust and accelerations from HST/WFC3-UVIS F350LP net counts via transformations from photometry to cross-section, dust mass, mass-loss rate, and thrust. We explicitly document the uncertainties through background handling, phase-function systematics, and geometric degeneracies along the line of sight. For U.T. 2025-11-30.80903, Jet2 is aligned with the projected transverse direction to within $\sim 0.5°$, while Jet3 is the closest to the projected normal direction with a moderate offset ($\sim 25°$). For UT 2025-12-27, Jet2 exhibits a monotonic PA drift over $\sim$ 24 minutes with a larger oscillation amplitude. The results provide a reproducible RTN-projection workflow and compact jet–RTN correspondence tables suitable for non-gravitational acceleration modeling of 3I/ATLAS.

Keywords: comets: general — interstellar objects — methods: data analysis — techniques: image processing — celestial mechanics

1. INTRODUCTION

The interstellar object 3I/ATLAS showed persistent inner-coma jet structures, with evolving position angles (PAs) and multiple periodicities, as reported in Scarmato & Loeb (2026). In cometary dynamics, non-gravitational accelerations are commonly expressed in the RTN (radial, transverse, normal) frame relative to the Sun as

$$a_{\rm NG}(t) = A_1\hat{R} + A_2\hat{T} + A_3\hat{N} \qquad (1)$$

where $\hat{\mathbf{R}}$ is the unit vector radial relative to the Sun, $\hat{\mathbf{T}}$ is transverse along the nucleus trajectory and $\hat{\mathbf{N}}$ is normal to the orbital plane. Here we link the observed jet directions to these components using sky-plane RTN projections and provide order-of-magnitude thrust estimates from HST photometry. This manuscript follows on the results reported in Scarmato & Loeb (2026), based on Hubble Space Telescope (HST) images available at MAST.

2. DATA AND INPUTS

2.1. *HST observations and jet PAs*

We adopted the observed jet PAs in the sky (with N=0°, E=90°) for UT 2025-11-30.80903:

- Jet1: $PA = 65°$,
- Jet2: $PA = 290°$,
- Jet3: $PA = 175°$.

At UT 2025-12-27.68194, Jet2 is measured at $PA \simeq 255°$ and shows a short-timescale drift in a sequence: 263°, 260°, 258°, 256°, 255° (each ±3°). As reported in Scarmato & Loeb (2026), Jet2 oscillates within roughly ±20° around $\sim 270°$.

2.2. *Astrometry and auxiliary angles*

For UT 2025-11-30.80903 we use:

- Pointing: RA=12:05:18, Dec=+00:08:52 (J2000),
- Solar PA: $PA_\odot = 113°$ ($PA_{\text{anti-Sun}} = 293°$),

- Apparent motion rates: $\dot{\alpha} = -2.18''\,\mathrm{h}^{-1}$, $\dot{\delta} = +0.77''\,\mathrm{h}^{-1}$, where $\dot{\alpha}$ and $\dot{\delta}$ denote the apparent rates of motion in right ascension and declination, respectively, projected on the sky plane. (motion PA $\approx 289°$).

For UT 2025-12-27 (image sequence) we use:

- Pointing: RA=10:09:02, Dec=+10:07:03 (J2000),
- Solar PA: $PA_{\odot} = 105°$ ($PA_{\text{anti-Sun}} = 285°$).

2.3. *HST photometric calibration and dynamics assumptions*

We adopt WFC3/UVIS drc parameters as used in the associated calculations:

- Filter: F350LP, exposure time $t_{\text{exp}} = 270$ s,
- Gain: 1.5 e^-/DN,
- PHOTFLAM: $5.24350573 \times 10^{-20}$ erg s^{-1} cm^{-2} Å^{-1} per (e^-/s),
- PHOTPLAM: 5851.1484 Å,
- Pixel scale: $0.04''$/px, aperture radius: 5 px ($0.20''$).

For thrust estimates we assume:

- Dust speed $v_d = 120$ m/s, gas speed $v_g = 400$ m/s, gas-to-dust mass-loss ratio $\chi = 1$,
- Nucleus radius $R_N = 1.3$ km and bulk density $\rho_N = 500$ kg m^{-3},
- Dust bulk density $\rho_d = 1000$ kg m^{-3} and effective grain size $a_{\text{eff}} = 10\,\mu$m (results scale linearly with a_{eff}),
- Dust phase function: Halley–Marcus (HM) at $\alpha \simeq 65°$ (see Section 3.3).

We emphasize that these are order-of-magnitude assumptions; the resulting accelerations carry factor is of few systematics, dominated by dust phase function and size distribution. The adopted parameters for the thrust estimates (dust velocity v_d, gas velocity v_g, gas-to-dust ratio χ, grain size a_{eff}, and densities) are chosen to be representative of typical cometary conditions reported in the literature.

In particular, the adopted dust and gas velocities are consistent with values commonly inferred for moderately active comets at heliocentric distances of a few AU, while the assumed grain size and densities correspond to standard order-of-magnitude estimates used in dust coma modeling.

We emphasize that these parameters are not uniquely constrained for 3I/ATLAS, and the resulting thrust and acceleration estimates should be interpreted as order-of-magnitude values. The derived quantities scale linearly with the assumed grain size and depend inversely on the adopted phase function and albedo.(e.g., A'Hearn et al. 1995; Jewitt & Meech 1987; Combi et al. 2004)

3. METHODS

3.1. *RTN construction and sky-plane projection*

Given heliocentric state vectors $(\mathbf{r}, \mathbf{v})$, we define

$$\hat{\mathbf{R}} = \frac{\mathbf{r}}{|\mathbf{r}|}, \qquad \hat{\mathbf{N}} = \frac{\mathbf{r} \times \mathbf{v}}{|\mathbf{r} \times \mathbf{v}|}, \qquad \hat{\mathbf{T}} = \hat{\mathbf{N}} \times \hat{\mathbf{R}}. \quad (2)$$

For a given observer pointing (RA, Dec), the line-of-sight unit vector is $\hat{\boldsymbol{\ell}}$. We project any unit vector $\hat{\mathbf{u}}$ to the plane of the sky via

$$\hat{\mathbf{u}}_{\perp} = \hat{\mathbf{u}} - (\hat{\mathbf{u}} \cdot \hat{\boldsymbol{\ell}})\hat{\boldsymbol{\ell}}. \quad (3)$$

The sky-plane position angle $PA(\hat{\mathbf{u}})$ (N=0°, E=90°) is then computed from $\hat{\mathbf{u}}_{\perp}$ expressed in the local tangent basis (North, East). A critical diagnostic is the projected norm $\|\hat{\mathbf{u}}_{\perp}\|$: if $\|\hat{\mathbf{R}}_{\perp}\| \ll 1$, then the radial direction is nearly along the line of sight and $PA(\hat{\mathbf{R}})$ is not diagnostically constrained.

3.2. *Photometry thrust pipeline*

For each jet region, the net DN sum (assumed already background/coma-subtracted) is converted to a count-rate

$$\dot{N} = \frac{\mathrm{DN_{net}}\,(\mathrm{GAIN})}{t_{\text{exp}}} \quad [\mathrm{e}^-\,\mathrm{s}^{-1}], \quad (4)$$

and to a flux density at the pivot wavelength

$$F_{\lambda} = \dot{N}\ \mathrm{PHOTFLAM}. \quad (5)$$

$\mathrm{DN_{net}}$ represents the background-subtracted detector signal in data numbers within the selected aperture. The detector gain converts data numbers to electrons via $N_{\mathrm{e}^-} = \mathrm{DN} \times \mathrm{GAIN}$, allowing the determination of the count rate $\dot{N}$ in electrons per second.

The conversion from count rate to physical flux density is performed using the PHOTFLAM calibration keyword, which provides the inverse sensitivity (i.e., the flux density corresponding to a count rate of 1 e^- s^{-1}). This procedure follows the standard HST/WFC3 photometric calibration pipeline (Dressel 2022), Wide Field Camera 3 Instrument Handbook, Version 14.0 (Baltimore: STScI). We estimate the dust scattering cross-section C (at order-of-magnitude) via a reflected-sunlight approximation:

$$C \propto \frac{r^2\Delta^2}{p\,\Phi(\alpha)}\,10^{-0.4(m-m_{\odot})}, \quad (6)$$

where p is geometric albedo, $\Phi(\alpha)$ is the dust phase function, and (r, Δ, α) are heliocentric distance, observer distance, and phase angle.

The proportionality in Eq. (6) reflects the use of an order-of-magnitude reflected-light approximation. The absolute normalization depends on the adopted solar magnitude and filter bandpass, and therefore introduces an additional systematic uncertainty of order unity in the derived cross-section.

For a single adopted grain size,

$$M_d \approx \frac{4}{3}\rho_d\, a_{\rm eff}\, C. \tag{7}$$

Assuming that the material leaves the observed aperture over a residence time $t_{\rm res} \approx \rho/v_d$, we estimate

$$\dot{m}_d \approx \frac{M_d}{t_{\rm res}}. \tag{8}$$

Including gas momentum with ratio $\chi = \dot{m}_g/\dot{m}_d$, the thrust is approximated as

$$F \approx \dot{m}_d\,(v_d + \chi v_g), \tag{9}$$

and the resulting acceleration magnitude is

$$|a| \approx \frac{F}{M_N}, \qquad M_N = \frac{4\pi}{3}R_N^3\rho_N. \tag{10}$$

Equation (9) approximates the combined dust and gas momentum contribution.

3.3. *Phase-function systematics at $\alpha \sim 65°$*

A key inconsistency encountered is the dust phase function choice at large phase angles. A simplistic linear law $\Phi_{\rm lin}(\alpha) = 10^{-0.4\beta\alpha}$ (with $\beta \simeq 0.04$ mag/deg) yields $\Phi_{\rm lin} \approx 0.09$ at $\alpha \simeq 65°$, whereas the Halley–Marcus (HM) composite phase function tabulated by the Lowell Observatory [1] gives $\Phi_{\rm HM} \approx 0.356$ at $\alpha \simeq 65°$. Because C, M_d, thrust, and $|a|$ scale as $1/\Phi$, adopting HM reduces these quantities by a factor $\Phi_{\rm lin}/\Phi_{\rm HM} \approx 0.26$ relative to the linear law. The HM composite dust phase function is adopted to account for the angular dependence of light scattering by cometary dust. This empirical function, derived from observations of comet 1P/Halley and subsequent datasets, provides a more realistic description of dust scattering compared to a simple linear phase law, particularly at intermediate phase angles ($\alpha \sim 60°$–$70°$).

At the phase angle relevant to this work ($\alpha \simeq 65°$), the HM phase function yields $\Phi_{\rm HM} \approx 0.356$, significantly larger than the value $\Phi_{\rm lin} \approx 0.09$ obtained from a linear phase law with $\beta \sim 0.04$ mag deg^{-1}. Since the derived dust cross-section, mass, and thrust scale as $1/\Phi(\alpha)$, the choice of phase function introduces a systematic factor of ~ 4 in the resulting physical quantities.

We therefore adopt the HM phase function as a more physically representative description of cometary dust scattering, while noting that phase-function uncertainties remain one of the dominant sources of systematic error (e.g., Schleicher et al. 1998; Marcus 2007; Schleicher & Bair 2011; see also Lowell Observatory dust phase function documentation). We note that the choice of phase function represents one of the dominant sources of systematic uncertainty, as all derived quantities scale as $\Phi^{-1}(\alpha)$. Alternative phase-function prescriptions would therefore shift the inferred cross-sections, masses, and accelerations by factors of a few.

4. RESULTS

4.1. *RTN sky-plane PA comparison (UT 2025-11-30.80903)*

Using the heliocentric state vector at JD 2461010.30903 and the pointing RA=12:05:18, Dec = +00:08:52, we obtained:

$$PA(\hat{\mathbf{T}}) = 290°, \qquad PA(\hat{\mathbf{N}}) = 200°, \tag{11}$$

while $\|\hat{\mathbf{R}}_\perp\| \approx 1.9 \times 10^{-4}$, implying that $\hat{\mathbf{R}}$ is nearly along the line of sight and $PA(\hat{\mathbf{R}})$ is not robust. With $PA_\odot = 113°$ the antisolar PA is 293°, nearly coincident with $PA(\hat{\mathbf{T}})$ in projection. Consequently, single-epoch PA matching cannot uniquely separate A_1 vs A_2 in this geometry, but the observed alignment is consistent with a significant contribution of A2, although a residual degeneracy with the radial component cannot be excluded given the near line-of-sight orientation of $\hat{R}$.

4.2. *RTN sky-plane PA comparison (UT 2025-12-27)*

For JD 2461036.5 and pointing RA=10:09:02, Dec = + 10:07:03, we obtained the following.

$$PA(\hat{\mathbf{T}}) = 287.6°, \qquad PA(\hat{\mathbf{N}}) = 197.6°, \tag{12}$$

and again $\|\hat{\mathbf{R}}_\perp\| \sim 10^{-4}$, implying that $PA(\hat{\mathbf{R}})$ is not diagnostically constrained. With $PA_\odot = 105°$, the antisolar PA is 285°.

4.3. *Compact jet table: PA offsets and order-of-magnitude accelerations*

Table 1 summarizes jet PAs, their angular offsets relative to the antisolar direction (A1 proxy), projected transverse (A2) and projected normal (A3), together with the order-of-magnitude accelerations derived from the photometry-to-thrust pipeline under the adopted assumptions.

[1] https://asteroid.lowell.edu/comet/dustphase/table

Table 1. Compact 2D jet–RTN correspondence and acceleration estimates (HM phase function, $a_{\rm eff} = 10\,\mu$m).

Jet	$\mathrm{DN}_{\rm net}$	PA (deg)	$\Delta A1$ (deg)	$\Delta A2$ (deg)	$\Delta A3$ (deg)	C (km^2)	M_d (kg)	$\dot{m}_d$ (kg/s)	F (N)	a (m/s^2)	Best match
Jet1	2.86e5	65	132	135.5	134.5	9.66	1.29e5	5.51e1	2.87e4	6.21e-9	—
Jet2	7.98e5	290	3	0.5	90.5	26.99	3.59e5	1.54e2	8.01e4	1.74e-8	A1,A2 (R,T)
Jet3	1.12e5	175	118	114.5	24.5	3.78	5.04e4	2.16e1	1.12e4	2.44e-9	A3 (weak)

NOTE—Angles are computed for UT 2025-11-30.80903 using $PA_{\text{anti-Sun}} = 293°$, $PA(\hat{\mathbf{T}}) = 289.54°$, $PA(\hat{\mathbf{N}}) = 199.54°$. The radial direction is near the line of sight ($\|\hat{\mathbf{R}}_\perp\| \ll 1$), so A1 cannot be uniquely validated by PA matching at this geometry. Acceleration estimates assume net DN already background/coma-subtracted and scale linearly with $a_{\rm eff}$ and inversely with $p\,\Phi(\alpha)$.

4.4. *Documented inconsistencies and their resolution*

We encountered and resolved the following issues during the analysis:

1. **Background treatment (DN):** Early calculations subtracted an additional background term even when DN values were already provided as net jet counts, artificially reducing fluxes and accelerations. The final tables treat jet DN values as net (no further subtraction).

2. **Phase function at $\alpha \simeq 65°$:** Switching from the linear phase law to the Halley–Marcus composite function reduces C, M_d, F, and a by a factor ~ 0.26 at $\alpha \simeq 65°$. We adopt HM for consistency.

3. **A1 vs A2 degeneracy in sky-plane:** At both epochs examined, $\|\hat{\mathbf{R}}_\perp\| \sim 10^{-4}$–$10^{-3}$, so the projected radial direction is nearly undefined. This makes A1 difficult to constrain from sky-plane PAs and can cause the antisolar direction to appear nearly coincident with $\hat{\mathbf{T}}$ in projection.

4. **Jet2 non-stationarity:** Multi-epoch PA differences for Jet2 are consistent with a wobble envelope ($\pm 20°$ around the mean PA), so a single PA should not be treated as a fixed inertial direction. RTN association should consider the oscillation envelope and/or a rotation-averaged thrust direction.

5. DISCUSSION: TOWARD A 3D (A1,A2,A3) DECOMPOSITION

A full 3D decomposition requires the jet unit vector $\hat{\mathbf{j}}(t)$, not only its sky-plane PA. Each PA provides a 3D plane constraint containing the line of sight; multiple epochs can recover a 3D cone/axis model for $\hat{\mathbf{j}}(t)$. Once $\hat{\mathbf{j}}(t)$ is estimated, the RTN components follow from dot products:

$$A_1 \propto \hat{\mathbf{j}} \cdot \hat{\mathbf{R}}, \qquad A_2 \propto \hat{\mathbf{j}} \cdot \hat{\mathbf{T}}, \qquad A_3 \propto \hat{\mathbf{j}} \cdot \hat{\mathbf{N}}. \tag{13}$$

The present 2D results already provide strong evidence that Jet2 contributes substantially to A_2 (transverse) at 2025-11-30, while Jet3 is only a weak/moderate candidate for A_3 based on PA proximity to $\hat{\mathbf{N}}$. In this context, the inferred alignment between jet directions and RTN components should be interpreted as a time-averaged effect, reflecting both rotational modulation and projection effects, rather than a strictly fixed forcing direction.

6. JET PERIODICITIES AND FREQUENCY RELATIONS

Scarmato & Loeb (2026) reports three distinct jet PA modulation periods, which we denote P_{J1}, P_{J2}, and P_{J3} for Jets 1–3, respectively. Using the values $P_{J1} = 2.9$ h, $P_{J2} = 7.1$ h, and $P_{J3} = 4.9$ h, the corresponding frequencies are

$$f_k = \frac{1}{P_k} \qquad [\mathrm{h}^{-1}]. \tag{14}$$

Numerically,

$$f_{J1} = 0.35, \quad f_{J2} = 0.14, \quad f_{J3} = 0.20\ \mathrm{hr}^{-1}. \tag{15}$$

A noteworthy relation is that the Jet 1 frequency is consistent with the sum of the Jet 2 and Jet 3 frequencies:

$$f_{J1} \simeq f_{J2} + f_{J3} \quad \Rightarrow \quad \frac{1}{2.9\ \mathrm{hr}} \simeq \frac{1}{7.1\ \mathrm{hr}} + \frac{1}{4.9\ \mathrm{hr}}, \tag{16}$$

since

$$f_{J2}+f_{J3} = 0.35\,\mathrm{hr}^{-1} \quad \Leftrightarrow \quad P_{\rm sum} = \frac{1}{f_{J2}+f_{J3}} = 2.90\,\mathrm{hr}, \tag{17}$$

Table 2. Jet periods and derived frequencies, including sum/difference combinations.

Entry	P (hr)	$f = 1/P$ (hr^{-1})	Combination	$P_{\rm equiv}$ (hr)	Comment
Jet1	2.9	0.3448	—	—	observed
Jet2	7.1	0.1408	—	—	dominant wobble period
Jet3	4.9	0.2041	—	—	secondary period
$f_{J2} + f_{J3}$	—	0.3449	$f_{J2} + f_{J3}$	2.90	$\approx P_{J1}$ (sum sideband)
$\lvert f_{J3} - f_{J2}\rvert$	—	0.0632	$\lvert f_{J3} - f_{J2}\rvert$	15.81	predicts ∼15.8 hr (difference sideband)

NOTE—Frequencies are computed from the jet PA modulation periods reported in Scarmato & Loeb (2026).

which matches P_{J1} within rounding. This type of linear frequency combination is naturally produced when the jet morphology is modulated by more than one physical timescale (e.g., non-principal-axis rotation with two fundamental modes producing sum/difference sidebands), or by geometric/visibility effects that mix two underlying periodicities. In the RTN framework developed here, such multi-period modulation implies that a single-epoch PA cannot be treated as a fixed inertial jet direction; instead, the relevant forcing direction should be considered as a time-dependent cone (or an average over rotational phase), while the magnitude of the forcing can be tracked via the photometry-to-thrust pipeline.

These results suggest that the observed jet activity may be linked to a complex rotational state of the nucleus, potentially involving non-principal-axis rotation or time-variable active regions. This relation should be regarded as suggestive rather than conclusive, as a detailed dynamical model would be required to establish a firm physical interpretation of the observed frequency combinations.

7. CONCLUSIONS

In this paper we provided: (i) a reproducible RTN sky-projection framework, (ii) a compact jet–RTN correspondence table, and (iii) order-of-magnitude non-gravitational accelerations derived from HST photometry under stated assumptions, while documenting the principal sources of uncertainty and degeneracy. The analysis supports Jet2 as the dominant contributor to transverse non-gravitational acceleration, forcing A2 in the examined geometry, with A1 generally not diagnosable from PA when $\hat{\mathbf{R}}$ is nearly along the line of sight. Future work should fit a 3D cone model for each jet using multi-epoch PA sequences to obtain robust (A_1, A_2, A_3) decompositions.

ACKNOWLEDGMENTS

A.L. was supported in part by the Harvard Black Hole Initiative (funded by GBMF and JTF) and Galileo Project. This work was carried out using Astroart for image processing, Astrometrica for time photometry, open-source Python tools for time-series analysis and figure generation, including Astropy, Numpy, Scipy and MatPlotlib. The authors thank NASA, ESA, and STScI for the HST data used in this work.

REFERENCES

A'Hearn, M. F., Millis, R. L., Schleicher, D. G., Osip, D. J., & Birch, P. V. 1995, Icarus, 118, 223

Combi, M. R., Harris, W. M., & Smyth, W. H. 2004, in Comets II, ed. M. C. Festou, H. U. Keller, & H. A. Weaver (Tucson, AZ: Univ. Arizona Press), 523

Dressel, L. 2022, Wide Field Camera 3 Instrument Handbook, Version 14.0 (Baltimore, MD: STScI)

Jewitt, D., & Meech, K. J. 1987, ApJ, 317, 992

Marcus, J. N. 2007, Int. Comet Q., 29, 39

Marsden, B. G., Sekanina, Z., & Yeomans, D. K. 1973, AJ, 78, 211

Schleicher, D. G., Woodney, L. M., & Millis, R. L. 1998, Icarus, 132, 397

Schleicher, D. G., & Bair, A. N. 2011, AJ, 141, 177

Scarmato, T., & Loeb, A. 2026, arXiv:2602.18512

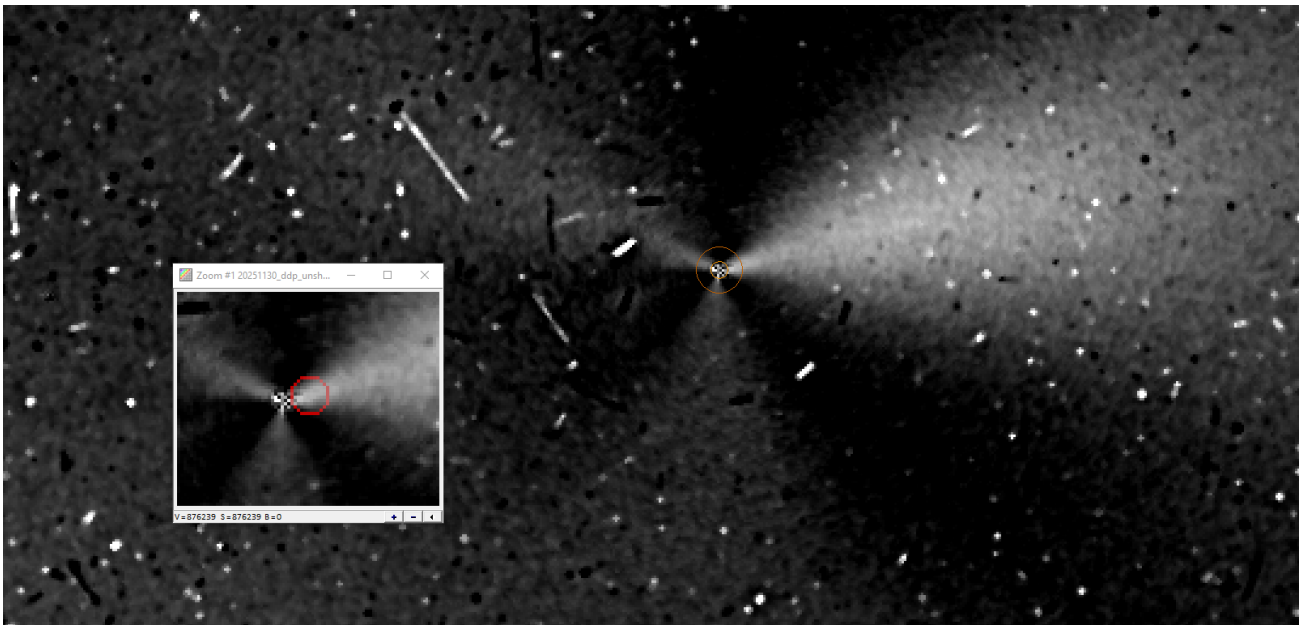

Figure 1. Reference inner-coma morphology showing persistent jet structures (illustrative). North is up and East is to the left. The RTN-mapping procedure uses the measured jet PAs and the astrometric pointing to compare with projected RTN directions computed from state vectors.